Research paper

ZrO$_2$ support imparts superior activity and stability of Co catalysts for CO$_2$ methanation

Wenhui Li[a], Xiaowa Nie[a], Xiao Jiang[c], Anfeng Zhang[a], Fanshu Ding[a], Min Liu[a], Zhongmin Liu[b], Xinwen Guo[a,*], Chunshan Song[a,c,*]

[a] State Key Laboratory of Fine Chemicals, PSU-DUT Joint Center for Energy Research, School of Chemical Engineering, Dalian University of Technology, Dalian, 116024, PR China
[b] National Engineering Laboratory for Methanol to Olefins, Dalian National Laboratory for Clean Energy, Dalian Institute of Chemical Physics, Chinese Academy of Sciences, Dalian, 116023, PR China
[c] Clean Fuels & Catalysis Program, EMS Energy Institute, PSU-DUT Joint Center for Energy Research, Departments of Energy and Mineral Engineering and of Chemical Engineering, The Pennsylvania State University, University Park, PA, 16802, USA

ARTICLE INFO

ABSTRACT

Screening of various supports reveals that Co catalysts supported on ZrO$_2$ and Al$_2$O$_3$ show good initial activity for CO$_2$ methanation. Co/ZrO$_2$ and Co/Al$_2$O$_3$ catalysts prepared by impregnation with different metal loadings were further examined comparatively. The 10Co/ZrO$_2$ catalyst showed high activity with CO$_2$ conversion of 92.5% and CH$_4$ selectivity of 99.9% without deactivation after 300 h time on stream (TOS). However, the 10Co/Al$_2$O$_3$ catalyst gave a lower CO$_2$ conversion of 77.8% which decreased to 38.6% after 300 h TOS. The catalysts were characterized by STEM/EDS (scanning transmission electron microscopy/energy-dispersive X-ray spectroscopy), in situ XRD(X-ray diffractometer), H$_2$-TPR(temperature programmed reduction), XPS (X-ray photo-electron spectroscopy), chemisorption of H$_2$, CO, CH$_4$, CO$_2$ and NH$_3$-TPD (temperature programmed desorption). Re-dispersion of Co species on the ZrO$_2$ support during reduction by H$_2$ was observed by STEM/EDS. New Co-Zr phase formed on the Co-ZrO$_2$ interface was directly observed by TEM for the first time; the Co/ZrO$_2$ catalyst exhibited high stability with high activity for CO$_2$ conversion. In situ XRD, H$_2$-TPR and XPS results indicate the promoting effect of ZrO$_2$ on the reduction of Co$_3$O$_4$ to Co metal along with the negative effect of Al$_2$O$_3$. The oxygen vacancies on the ZrO$_2$ detected by XPS may help to activate CO$_2$ and H$_2$O and resist deactivation. Co/Al$_2$O$_3$ catalyst deactivates rapidly due to coke deposition and spinel formation.

1. Introduction

Continuing consumption of fossil fuels worldwide led to increasing CO$_2$ concentration in the atmosphere, and global climate change caused by greenhouse gases dominated by CO$_2$ has become a major challenge [1–11]. At present, CO$_2$ can be reduced in three ways: control of CO$_2$ emissions, CO$_2$ capture and storage, and chemical conversion and utilization of CO$_2$ [5,7]. Carbon storage is important for cutting CO$_2$ emissions quickly but has issue of potential leakage of CO$_2$ [3,5]; CO$_2$ conversion requires energy input but is receiving increasing attention in conjunction with renewable energy utilization.

CO$_2$ hydrogenation [2,6,8,11] using H$_2$ produced with renewable energy sources [12,13] is a promising research direction to produce methanol [14–19], hydrocarbons [20–22], synthetic natural gas (methane) [23–29] and chemicals [30]. Currently uses of renewable energy

sources are limited by their inherent intermittency and require scalable means of storage [31]. Electrolysis of water to generate H$_2$ is a potential storage approach. Effective conversion of CO$_2$ to fuels and chemicals with renewable energy can be achieved using H$_2$ produced with renewable energy [32–34]. On the other hand, the above applications for CO$_2$ methanation also require inexpensive and stable catalysts with high performance.

CO$_2$ methanation was first reported by the French chemist Paul Sabatier [35]. This reaction with inexpensive and stable catalysts is a promising new way to store renewable energy such as wind and solar power, to transform biogas effectively to biomethane and to convert CO$_2$ to chemical feedstock and fuel [36,37]. CO$_2$ methanation is exothermic with high equilibrium conversion between 25 °C to 400 °C as shown in Fig. 1 which is plotted using the data from literature [38,39].

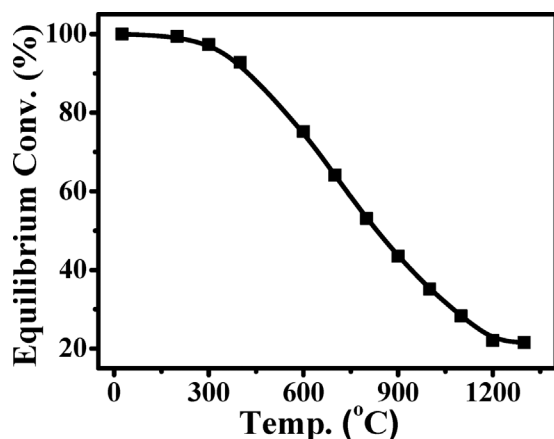CO$_2$ methanation can be catalyzed by transition metals such as Co

Fig. 1. Equilibrium conversion of CO_2 in methanation at different temperatures.

[40–43], Ni [44,45], Ru [46,47], Rh [48] and Pd [49,50]. Co and Ni-based catalysts are preferred because of their low costs compared with the noble metals (Ru, Rh, Pd). Weatherbee and Bartholomew studied various Group VIII metal catalysts supported on SiO_2 and found Co is more active than Ni in CO_2 methanation [51]. Other researchers have used Al_2O_3 [27,52], SiO_2 [53,54], ZrO_2 [55], TiO_2 [26,56], CeO_2 [25] and zeolites [44] to support Ni or Co [41,42,57] to catalyze methanation of synthesis gas or CO_2. Among the results reported so far, only a few Co-based catalysts show high CO_2 conversion [41,42], high selectivity to CH_4 and long lifetime at the same time. There are many factors concerning supports that can influence the performance of metal catalysts [58], such as pore size [59], structure of supports [41], surface chemistry and metal-support interaction [45,60–62]. The activity and selectivity of these catalysts have been shown to be sensitive to the interaction between the active metals and oxide supports [45,60–62]. Previous studies suggested that the reduction of CO_2 requires the co-operation of metal which can dissociate H_2, and the metal-support interface which can activate CO_2 [47,50]. Therefore, the support and reduction degree of the metal oxide affect the activity of the catalysts. Schulz et al. found that the right amount of zirconium oxide was conducive to the reduction of cobalt [63]. Oukaci et al. reported that Zr played an important role in moderating Co-support interactions and improving the catalyst stability [64]. ZrO_2 may contain both weak acid sites and basic sites and have different phases [65]. The higher concentration of oxygen defects on the m-ZrO_2 could improve the adsorption of oxygenated species including CO_2 [66,67]. In addition, ZrO_2 has excellent hydrothermal stability to adapt to the high temperature and high pressure of CO_2 methanation [68]. ZrO_2 is frequently used as a promoter [55]. The γ-Al_2O_3 is commonly used as an oxide support and known for its strong metal-support effect [22]. There have been some theoretical studies examining the effect of supports on the performance of metal catalysts [69–76], and these studies illustrate that the metal-support interaction plays a very important role in the activity and selectivity.

Despite these efforts, the substantial differences between ZrO_2- and Al_2O_3-supported catalysts including adsorption and activation of reactants, influence on metal oxide reducibility and catalytic properties have not been fully studied. Understanding the influence of the support on the metal nanoparticles has been an important issue in heterogeneous catalysis for decades [77].

In the present work, various supports including ZrO_2, Al_2O_3, SiO_2, SiC, TiO_2 and activated carbon (AC) loaded with 10 wt% Co were first screened in CO_2 methanation. The Co/ZrO_2 catalyst has the highest CH_4 yield, while Al_2O_3 is the most studied support. The Co/ZrO_2 catalyst shows both a high CO_2 conversion (close to the equilibrium) and high stability. No deactivation is observed after 300 h on $10Co/ZrO_2$, but on $10Co/Al_2O_3$, CO_2 conversion decreased rapidly from 77.8% to 36.8%

after 300 h. Another aim of the present work is to address the following questions: Why is the cobalt on ZrO_2 more easily reduced? Why is the ZrO_2 supported Co catalyst more active? Why does the $10Co/Al_2O_3$ catalyst deactivate rapidly?

2. Experimental section

2.1. Catalysts preparation

Nano monoclinic ZrO_2 and γ-Al_2O_3 were used as the support materials. γ-Al_2O_3 was obtained after calcining pseudo-boehmite in a Maffler furnace in air at 400 °C for 4 h. ZrO_2 samples were prepared by dissolving $ZrO(NO_3)_2 \cdot 2H_2O$ (> 45% ZrO_2, Aladdin Chemicals) in a mixture (ca. 70 ml) of urea (> 99%, Aladdin Chemicals) and deionized water, followed by the thermal treatment in a Teflon-lined stainless-steel autoclave (ca. 100 ml) at 160 °C under autogenous (self-generated) pressure for 20 h. The concentration of Zr^{4+} in the solution was 0.4 M, and the urea/Zr^{4+} molar ratio was 10. The resulting precipitate was washed thoroughly with water and dried at 110 °C overnight in ambient air and then calcined at 400 °C for 4 h in dry air [78]. Co/ZrO_2 and Co/Al_2O_3 catalysts were prepared by the impregnation method using aqueous solution of $Co(NO_3)_2 \cdot 6H_2O$ (> 99%, Aladdin Chemicals) with Co loadings of 2, 10, and 15 wt%. The impregnated samples were dried at 120 °C for 12 h and calcined at 500 °C for 4 h with heating rate at 2 °C min^{-1}. The catalysts prepared in this work are denoted as (x) Co/Al_2O_3 or (x) Co/ZrO_2, where x represents the mass fraction of the Co metal on the basis of support weight.

2.2. Catalytic test

The catalytic hydrogenation of CO_2 was carried out in a pressurized fixed-bed flow reactor (inner diameter 8 mm) where a weighed 1 g catalyst (10–20 mesh) was loaded for each test. Prior to the reaction, the catalyst was pre-reduced in H_2 at 400 °C overnight. After the reduction, the feed gas was switched to the mixture of CO_2 and H_2 with H_2/CO_2 molar ratio of 4 under pressure of 3 MPa at 400 °C; the space velocity was 3600 ml g^{-1}h^{-1}.

The products were analyzed on-line by a gas chromatograph (FULI GC 97). CO_2, CO and CH_4 were analyzed on a carbon molecular sieve column with a thermal conductivity detector (TCD). The conversion of CO_2 and CH_4 selectivity were calculated as Eq. (1) and (2):

$$CO_2\, Conversion\, (\%) = \frac{n_{co_2\,,in} - n_{co_2\,,out}}{n_{co_2\,,in}} \times 100\% \quad (1)$$

$$CH_4\, Selectivity\, (\%) = \frac{n_{CH_4\,,out}}{n_{co_2\,,in} - n_{co_2\,,out}} \times 100\% \quad (2)$$

where $n_{co_2\,,in}$ and $n_{co_2\,,out}$ represent the molar concentration of CO_2 in the feed and effluent, respectively; $n_{CH_4\,,out}$ represents the molar concentration of CH_4 in the effluent.

2.3. Characterization of catalysts

The textural properties of the samples were determined by N_2 adsorption on a Quantachrome AUTO-SORB-1-MP sorption analyzer at liquid nitrogen temperature. Prior to the measurements, the samples were degassed at 350 °C for 2 h. The specific surface area was determined by the Brunauer-Emmett-Teller (BET) method. The total pore volume was obtained from the amount of vapor adsorbed at a relative pressure (P/P_0) close to unity, where P and P_0 are the measured and equilibrium pressure, respectively. The pore size distribution was obtained using the adsorption isotherm through Barrett-Joyner-Halenda (BJH) method.

The morphological properties of Co-based catalysts were studied by high resolution transmission electron microscopy (TEM) and scanning TEM/energy-dispersive X-ray spectroscopy (STEM/EDS) using a FEI

Talos F200X TEM at an accelerating voltage of 200 kV. The calcined catalyst precursors were reduced on the fixed bed reactors under the reaction condition and then cool down to room temperature under the hydrogen. In order to avoid the oxidation of the reduced catalysts, passivating treatment had been done for the reduced catalysts. The samples were dispersed in ethanol and sonicated for 10 min. A few droplets of the supernatant liquid were dropped on a carbon-coated copper grid, followed by drying at ambient temperature. Prior to the STEM analysis the sample was subjected to a "beam shower" for ~ 30 min under the TEM beam to minimize any beam-induced carbon deposition on the surface of the Co-based catalysts during the STEM analysis. EDS maps were acquired in the Talos using Bruker Super-X quad EDS detectors at a beam current of 0.12 nA for approximately 3 min. A Standardless Cliff-Lorimer quantification was applied for the deconvolution of EDS line intensity using the Bruker Esprit software. High-resolution TEM imaging was conducted to obtain clear lattice fringes at the interface between the metal and support.

H_2-temperature programmed reduction (TPR) was conducted with ChemBETPulsar TPR/TPD equipment (Quantachrome, USA) to analyze the reducibility of the calcined catalysts. Prior to reduction, ~ 0.10 g of the calcined sample was charged into the quartz tube and flushed with high purity Ar at 300 °C for 1 h, followed by cooling down to room temperature. The TPR program was then initiated by switching to 5 vol% H_2/Ar with a total flow rate of 30 ml min^{-1} and heating up to 900 °C at 10 °C min^{-1}. A cooling trap was placed before the detector. Dispersion of cobalt particles was characterized by H_2 titration using the same equipment. Samples were reduced in H_2 at 400 °C for 2 h. After reduction, the gas was changed to high-purity Ar for desorption for 1 h and then allowed to cool down to 30 °C, followed by H_2 titration. The dispersion was estimated based on the assumption of H/Co = 1 [79,80].

H_2-temperature programmed desorption (TPD) was conducted (in the same equipment as TPR) with Ar as the carrier gas. About 0.10 g catalyst was charged into the quartz tube and reduced in 5 vol% H_2/Ar (ca. 30 ml min^{-1}) at 400 °C for 2 h. The catalyst bed was subsequently flushed with Ar (ca. 30 ml min^{-1}) for desorption for 30 min at the same temperature. Then, the sample was cooled down to 30 °C, followed by H_2 flow for 30 min (ca. 30 ml min^{-1}). After adsorption, the system was purged with argon gas (ca. 30 ml min^{-1}) for 30 min to remove weakly-adsorbed species. The TPD program was initiated by heating up to 450 °C with a rate of 10 °C min^{-1}. The resulting profile was monitored using TCD. CO_2-TPD, CO-TPD, CH_4-TPD and NH_3-TPD (8 vol% NH_3 in Ar) measurements were performed using the same equipment with similar procedure, wherein CO_2, CO, CH_4 and NH_3 were introduced as adsorption gases (ca. 30 ml min^{-1}), respectively.

X-ray photoelectron spectra (XPS) were measured with a VG ESCALAB250 Spectrometer with a monochromatic Al-Kα (1486.6 eV) at 15 kV and 10 mA, and all binding energies were referenced to the C 1 s at 284.6 eV. The calcined catalyst precursors were reduced on the fixed bed reactors under the reaction condition and then cool down to room temperature under the hydrogen. In order to avoid the oxidation of the reduced catalysts, passivating treatment had been done for the reduced catalysts.

Thermogravimetric analysis (TGA) was conducted on a TGA/SDTA851e Thermobalance (Mettler Toledo). The sample weight was between 7 and 10 mg. The TGA data were collected in the range of 30–850 °C a rate of 10 °C min^{-1} in N_2 flow (ca. 25 ml min^{-1}). TG analysis was used to measure the weight difference of the catalysts after reaction.

XRD patterns of calcined catalyst precursors and spent catalysts were determined using a RigakuSmartLab (9) diffractometer with Cu Kα radiation (λ = 1.5406 Å) with 0.02 step size over the range between 5° and 80°. In situ XRD measurements were performed in the XRK 900 reactor chamber which was made by Anton Paar Corporation in order to observe the change of crystallite phases of the catalysts during the reduction process. The flakiness samples was tiled on the

ceramic sample stage (internal diameter 15 mm). There are beryllium windows on the hermetic reactor chamber allowing the X-ray through. The temperature was controlled from 50 to 750 °C by TCU 750 Temperature Control Unit. The patterns were determined on a RigakuSmartLab (9) diffractometer with Cu Kα radiation (λ = 1.5406 Å). The spectra were recorded over a 2θ range of 5–80° with a step size of 0.02°. The resultant XRD date was analyzed by the integrated software PDXL2.

Gases were supplied to the reactor chamber from an apparatus with calibrated mass-flow meters. Before starting the temperature program, 10 vol% H_2/Ar (ca. 60 ml/min) was introduced to discharge the air in the chamber for 30 min and then reduce the catalysts, followed by heating up the chamber from 50 to 750 °C with a rate of 50 °C in 30 min. In situ reaction pool has always maintained low pressure(ca. P < 0.1 MPa). It should be noted that the in situ XRD patterns showed shifts in peak positions compared to both full scans and tabulated values due to temperature-induced lattice expansion and different sample heights. These shifts in peak positions, which are not related to underlying physicochemical processes, were taken into consideration during peak assignments.

3. Results and discussion

3.1. Effects of supports on Co catalytic for CO_2 methanation

Table 1 shows the CO_2 conversion and CH_4 selectivity over Co catalysts with the metal loading fixed at 10 wt% on ZrO_2, Al_2O_3, SiO_2, SiC, TiO_2 and activated carbon (AC) in CO_2 methanation. As shown in Table 1, the ZrO_2-supported Co catalyst gave not only the highest CO_2 conversion but also the highest CH_4 selectivity. The Al_2O_3-, SiO_2-, SiC- and AC-supported Co catalysts show good CO_2 conversion and also high CH_4 selectivity. The TiO_2-supported Co catalysts did not exhibit acceptable CH_4 selectivity nor good CO_2 conversion. Razzaq *et al.* [27] have compared the Co/Al_2O_3 and CoN4/Al_2O_3 catalysts for the CO and CO_2 methanation at 400 °C. The CO_2 conversion was 75% at 400 °C which is similar to our experimental results with Al_2O_3- and SiC-supported Co catalysts in Table 1. Mesoporous Co/KIT-6 and Co/meso-SiO_2 catalysts with well-dispersed Co species were reported by Zhou et al. for CO_2 methanation which exhibited 46% and 36% CO_2 conversion at 260 °C and 360 °C, respectively [41,42]. Chen *et al.* [58] have tested PtCo bimetallic catalysts supported on TiO_2 and ZrO_2 for CO_2 hydrogenation. PtCo/TiO_2 catalyst effectively converts CO_2 an H_2 into CO but PtCo/ZrO_2 catalyze the selective formation of CH_4. Our subsequent studies focused on the Co/ZrO_2 in comparison with Co/Al_2O_3.

Fig. 2(a) illustrates the changes of CO_2 conversion (left) and CH_4 selectivity (right) as a function of time on stream (TOS) over (x)Co/ZrO_2 and (x)Co/Al_2O_3. Generally, the activity and stability of (x)Co/ZrO_2 catalysts are significantly better than those of the (x)Co/Al_2O_3 catalysts at same Co loadings. At 2 wt% Co loading, the CO_2 conversion and CH_4 selectivity are 82.5% and 99.8%, respectively, on the ZrO_2-supported catalyst during the first 20 h on stream; however, the

Table 1
The reaction performance of the catalysts in CO_2 methanation.[a]

Cat.	CO_2 Conv./%	Selectivity/%	
		CO	CH_4
10Co/ZrO_2	92.5	0.1	99.9
10Co/SiO_2	80.1	2.2	97.8
10Co/Al_2O_3	77.8	3.5	96.5
10Co/SiC	77.5	3.6	96.4
10Co/TiO_2	30.9	95.8	4.2
10Co/AC	40.5	9.2	90.8

[a] Conditions: molar ratio of H_2/CO_2 = 4/1, GHSV = 3600 ml g^{1}h^1,P = 3 MPa, T = 400 °C.
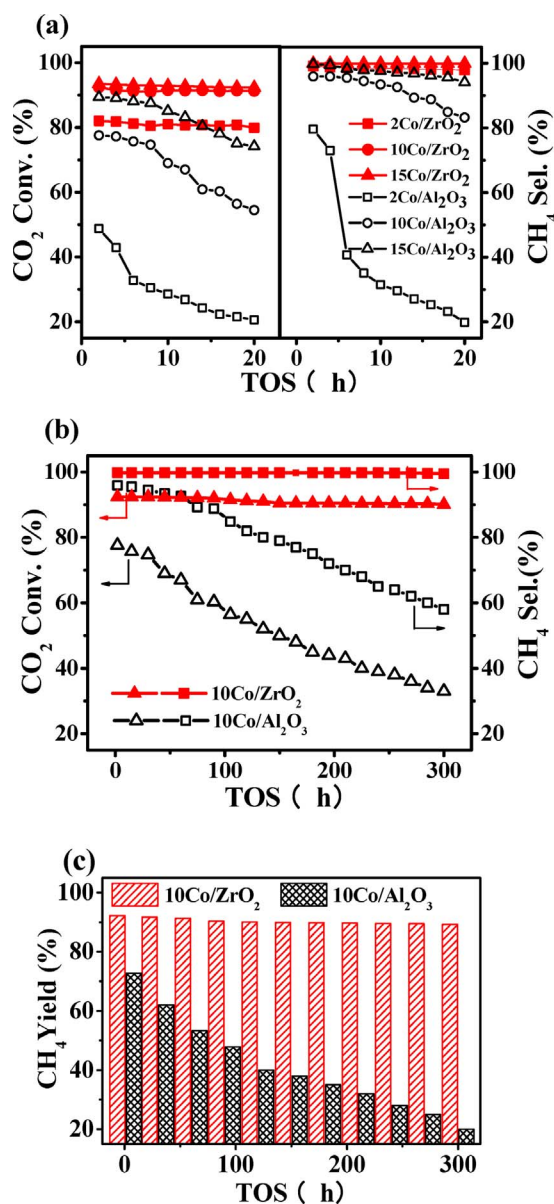
Fig. 2. (a) CO_2 conversion (left) and CH_4 selectivity (right) over the Co/ZrO_2 and Co/Al_2O_3 catalysts with different Co loadings after 20 h TOS, (b) CO_2 conversion and CH_4 selectivity over the $10Co/ZrO_2$ and $10Co/Al_2O_3$ after 300 h TOS, (c) CH_4 yield of the $10Co/ZrO_2$ and $10Co/Al_2O_3$ catalysts. Conditions: molar ratio of $H_2/CO_2 = 4/1$, GHSV = 3600 ml $g^{-1}h^{-1}$, P = 3 MPa, T = 400 °C.

corresponding values over Al_2O_3-supported catalyst are much lower, namely 49.5% and 79.8%, respectively. Upon increasing Co loading to 10 wt%, a further rise in CO_2 conversion is observed over both catalysts, as well as CH_4 selectivity. The conversion with $10Co/ZrO_2$ even approaches the equilibrium value (i.e., 92.5%), whereas it is only 77.8% on $10Co/Al_2O_3$. With a further increase of Co loading (i.e., 15 wt %), the gap of catalytic performances between ZrO_2-supported and Al_2O_3-supported catalysts becomes narrow. It is also worth noting that the ZrO_2-supported catalysts with lower Co loading (e.g., 2 wt%) exhibited higher activity and selectivity than the Al_2O_3-supported catalysts with higher or same Co loading (e.g., 10 wt%), indicating a much higher metal efficiency for the former than the latter.

Fig. 2(a) also revealed that the superior stability of (x)Co/ZrO_2 catalysts. However, (x)Co/Al_2O_3 gradually loses activities within the same range of TOS, the drop of which is particularly significant at lower Co loading. In order to further verify such a major difference of stability, long-term tests were conducted on both Co/ZrO_2 and Co/Al_2O_3
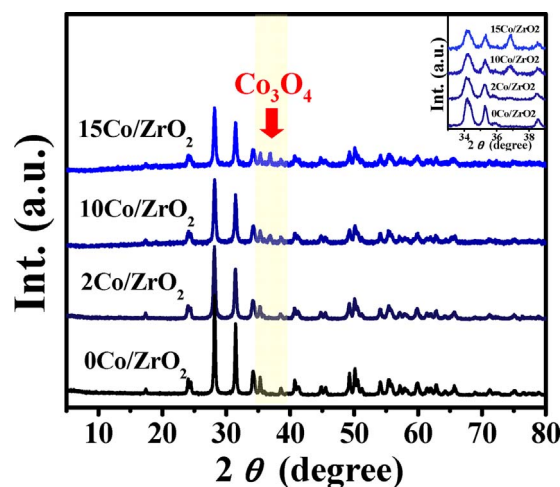

Fig. 3. XRD patterns of calcined catalyst precursors zirconia-supported cobalt catalysts with different loadings.

with 10 wt% Co loading, and the results are illustrated in Fig. 2(b). Clearly, the ZrO_2-supported catalyst still exhibits superior and stable activity even after 300 h TOS, in contrast, the Co/Al_2O_3 loses nearly 46% and 35% of its starting conversion and selectivity, respectively. Besides, the corresponding CH_4 yield is shown in Fig. 2(c). After 300 h TOS, the CH_4 yield of Co/ZrO_2 is still 90%, while yield loss of Co/Al_2O_3 is substantial, and the final value only accounts for approximately 1/5 of that over $10Co/ZrO_2$. Thus, in comparison to Co/Al_2O_3, the ZrO_2-supported Co catalysts revealed superior activity and selectivity in CO_2 methanation under the condition employed. More importantly, the activity of Co/ZrO_2 catalysts is extremely stable even after a long-term test.

3.2. Crystalline structure of the ZrO_2- and Al_2O_3-supported catalysts

The XRD patterns of the Co/ZrO_2 and Co/Al_2O_3 samples in the calcined forms are presented in Figs. 3 and 4, respectively. All ZrO_2-supported samples show two clear diffraction peaks centering at 28.1° and 31.5°, which are typical for the zirconia with monoclinic phase [78]. The diffraction peak centered at 36.8° appears for both ZrO_2- and Al_2O_3-supported catalysts and can be attributed to Co_3O_4 particles [81], and the intensity is enhanced with increasing Co loading. Additionally, two other peaks centered at 30.1° and 59.5°, can be observed for Co/Al_2O_3 catalysts and correspond to the $CoAl_2O_4$ spinel (see the top
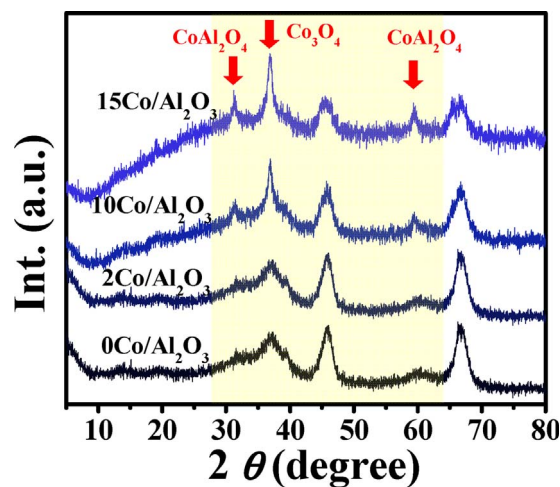

Fig. 4. XRD patterns of calcined catalyst precursors γ-Al_2O_3-supported cobalt catalysts with different loadings.

Table 2
Physico-chemical properties of cobalt catalysts.

Sample	Surface area [m^2g^{-1}]			Pore volume [cm^3g^{-1}]		Co_3O_4 size[a]	Dispersion[b]	Active metal[c]	TOF[d]
	S_{BET}	S_{micro}	S_{meso}	V_{pore}	V_{micro}	[nm]	[%]	[$*10^{-5}mol/g_{cat}$]	[s^{-1}]
$2Co/ZrO_2$	29	2.7	27.1	0.16	0.001	18	–	–	–
$10Co/ZrO_2$	27	1.0	26.5	0.17	0.001	22	6	5.1	0.20
$15Co/ZrO_2$	25	0.2	23.2	0.12	0.001	27	–	–	–
$2Co/Al_2O_3$	230	0	230	0.34	0	7	–	–	–
$10Co/Al_2O_3$	216	0	216	0.27	0	16	9	4.5	0.18
$15Co/Al_2O_3$	202	0	202	0.15	0	19	–	–	–

[a] The Co_3O_4 crystallite sizes were determined using Scherrer equation.
[b] Metal dispersion was determined by the H_2 titration analysis.
[c] Active metal = metal mole × reducibility × dispersion.
[d] TOF = (GHSV × 1/4/22.4 × CO_2 Conversion)/(metal mole × reducibility × dispersion)/t, the TOF data displayed on the Table 2 is correspond to the 1 h time on stream.

diffraction pattern of Fig. 4), the intensity of which increases with increasing Co loading. The $CoAl_2O_4$ spinel is regarded as non-active species in CO_2 hydrogenation [81] because in which the Co is hardly reduced. This is one of the reasons that Al_2O_3-supported catalysts exhibited lower activity compared to the ZrO_2-supported catalysts. The crystallite sizes determined using Scherrer equation are summarized in Table 2. Clearly, at the same Co loading, the average Co_3O_4 crystalline sizes in ZrO_2-supported catalysts are larger than those in Al_2O_3-supported catalysts.

Fig. 5 shows the in situ XRD patterns of the Co catalysts which reflect on the structural shifts of cobalt species during the H_2-TPR inside XRD chamber. Each test temperature was 50 °C apart and retained for 30 min with 60 ml/min of 10 vol% H_2/Ar. The diffraction peaks of Co_3O_4 oxide particles located at 36.8° become weaker with the programmed rise of reduction temperature, which is due to the reduction of Co_3O_4 to CoO particles. The reduction of Co_3O_4 oxide particles begins at 250 °C on ZrO_2 support while it is 350 °C on Al_2O_3 support. The peak located at 42.2° for CoO particles only stays for a short time and then transforms to metal Co^0 on the ZrO_2. In contrast, the CoO is reduced more slowly on Al_2O_3. The reduction is completed at 400 and 600 °C on ZrO_2 and Al_2O_3, respectively, as evidenced by the appearance of metal Co^0 diffraction peak (e.g., 44°). These observations demonstrate that cobalt species supported on ZrO_2 can be reduced completely at 400 °C in H_2, while at the same temperature, the reduction is only partial in the case of Al_2O_3. Thus, the poor reducibility and low reduction degree of the Co oxide on Al_2O_3 lead to insufficient active metal sites and their low activity.

3.3. Physical properties of Co/ZrO_2 and Co/Al_2O_3 catalysts

Physical properties of ZrO_2- and Al_2O_3-supported catalysts are summarized in Table 2 and the nitrogen adsorption-desorption isotherms of $10Co/ZrO_2$ and $10Co/Al_2O_3$ are illustrated in **Fig. S1**. Compared to Co/ZrO_2 catalysts, the BET surface areas of Co/Al_2O_3 catalysts are much larger. The physical properties are often related to the metal dispersion. The dispersion of Co was estimated using H_2 titration over two representative catalysts with same metal loading and also shown in Table 2. As expected, the $10Co/Al_2O_3$ exhibits higher metal dispersion (9%) than $10Co/ZrO_2$ (6%) due to the larger surface area of the former catalyst. This observation is also consistent with XRD data. From **Fig. S1**, mesopores are present on the Al_2O_3-supported catalyst.

3.4. Reduction behaviors

Fig. 6 shows the TPR profiles for $10Co/ZrO_2$ and $10Co/Al_2O_3$. The Co_3O_4 was used as a reference standard, which shows a peak at 456 °C, corresponding to the reduction of Co_3O_4 to Co. In the profile of $10Co/ZrO_2$, two distinct peaks centered at 372 and 420 °C were observed, which can be attributed to two-step reduction of Co_3O_4 to CoO and subsequently to Co, respectively [81–83]. The shoulder peak in high

temperature side of the second peak T_{420} corresponds to the reduction of cobalt species from the bulk phase [41,84]. Noticeably, the reduction temperature of the Co_3O_4 particles on the $10Co/ZrO_2$ (e.g., 372 °C) is even lower than that of Co_3O_4 oxide (e.g., 456 °C), indicating the enhanced reducibility of Co_3O_4 on ZrO_2 [59]. Sun et al. found that the reduction degree was enhanced with increasing Co_3O_4 size, and the Co-ZrO_2 interaction decreased with the increase of pore size [59]. On the other hand, the sequential reduction was observed on $10Co/Al_2O_3$ as well, except that the corresponding peaks shift to higher temperatures, namely 488 and 721 °C, respectively. This result is in agreement with the in situ XRD results. Such peak shift, in comparison to Co/ZrO_2, possibly originates from the difference of Co particle size over different supports.

As discussed in Section 3.2, the ZrO_2-supported catalysts exhibit larger particle size than the Al_2O_3-supported catalysts, and the reduction of the former catalysts is easier. Another possible reason derives from the formation of $CoAl_2O_4$ spinel on the Al_2O_3-suppported catalysts, which is evidenced from the XRD patterns. Such explanation is also supported by the estimated H_2 consumption areas on the TPR profiles, where the $10Co/ZrO_2$ consumes more H_2 than $10Co/Al_2O_3$. Therefore, the stability of spinel has a negative impact on the reduction of Co_3O_4. The surface of reduced metal particles should behave as active sites for CO_2 methanation [85]. The Co-ZrO_2 interaction improves the reducibility of Co and provides more active sites (Table 2).

3.5. Surface properties of catalysts

As discussed in Section 3.4, it is suggested that there exists a close interaction between Co metal and ZrO_2 support. In order to further confirm such interaction, XPS analysis was conducted. Fig. 7(a) depicts the XPS spectra in the Co 2p region for calcined catalyst precursors for Co/ZrO_2 and Co/Al_2O_3; the corresponding XPS data are summarized in Table 3. The spectra of both ZrO_2- and Al_2O_3-supported catalysts exhibit an intense doublet centering at 778.5 and 794.9 eV, along with two additional satellite peaks centering at 780.8 and 796.0 eV. The intense doublet, from low towards high BEs, can be attributed to Co $2p_{3/2}$ and Co $2p_{1/2}$, respectively [86]. Deconvolution for the Co $2p_{3/2}$ of $10Co/ZrO_2$ indicates the existence of Co^{2+} (ca. 778.5 eV) and Co^{3+} (ca. 780.8 eV), whose Co^{2+}/Co^{3+} atomic ratio is 73:27. On the other hand, the Co $2p_{3/2}$ peak of $10Co/Al_2O_3$ contains similar components, namely Co^{2+} (ca. 778.9 eV) and Co^{3+} (ca. 780.4 eV), and the atomic ratio of which is 47:53. Clearly, the higher atomic ratio of Co^{2+}/Co^{3+} for Co/ZrO_2 indicates a CoO-rich surface which further implies its better reducibility compared to Co/Al_2O_3. This observation is also in line with the TPR results as the reduction peaks of Co/ZrO_2 appear at lower temperatures, while those of the latter are retarded to higher temperatures. Thus, these XPS results assist in interpreting the reduction behavior of Co oxides over different supports as well.

Fig. 7(b) and (c) present the XPS spectra in the O1 s region for the same samples. The intense peak at 528.7–529.8 eV can be attributed to
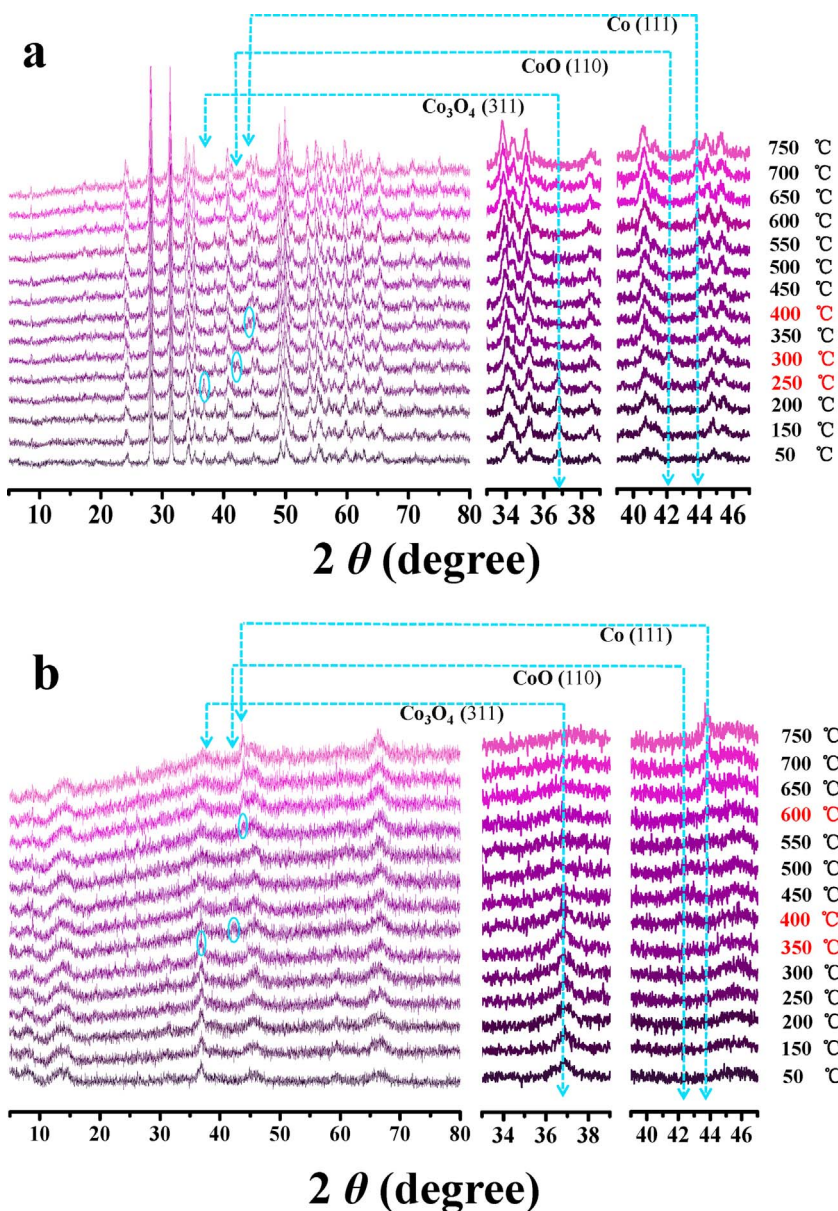
Fig. 5. In situ XRD patterns of cobalt catalysts (a) 10Co/ZrO$_2$ and (b) 10Co/Al$_2$O$_3$ during temperature-programmed reduction inside XRD chamber.
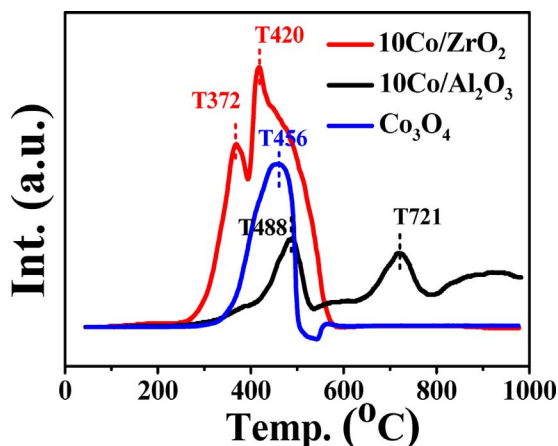

Fig. 6. H$_2$-TPR profiles of 10Co/ZrO$_2$, 10Co/Al$_2$O$_3$ and Co$_3$O$_4$.

the lattice oxygen in ZrO$_2$ or Al$_2$O$_3$, while the signals at 530.7–530.9 eV can be assigned to the surface hydroxyl groups or the adsorbed oxygen [87,88]. Based on the area integrals of the lattice oxygen (O$_\alpha$) and surface hydroxyl/adsorbed oxygen (O$_\beta$), the ratio of O$_\beta$ to O$_T$ (O$_T$ = O$_\alpha$ + O$_\beta$) for all samples was estimated and tabulated in Table 3. It can be seen that on the H$_2$-reduced 10Co/ZrO$_2$ the percentage of surface hydroxyl/adsorbed oxygen is approximately six times of that for the calcined catalyst precursors. The reduced 10Co/ZrO$_2$ exhibits higher ratio of O$_\beta$/O$_T$ than that of the calcined catalyst precursors (e.g., 24.0% vs 4.2%), implying a significant decrease of lattice oxygen O$_\alpha$ on this sample. In other words, such behavior could be ascribed to the increasing number of oxygen vacancies upon reduction. The ratio of O$_\beta$/O$_T$ is relatively stable after 8 h TOS, implying the stable surface property of this sample even under high-temperature and pressurized reaction conditions. It is also noticeable that the O$_\alpha$ of ZrO$_2$ shifts from 528.7 to 529.3 eV upon reduction, suggesting the existence of electron transfer between Co metal and ZrO$_2$ support. In contrast, the O$_\alpha$ peak of Al$_2$O$_3$ hardly shows any peak shift nor significant ratio variation, which, thereof, demonstrates a much weaker Co-Al$_2$O$_3$ interaction in comparison to the Co-ZrO$_2$. The slight increase of the surface hydroxyl on the spent 10Co/Al$_2$O$_3$ may be attributed to the adsorption of the
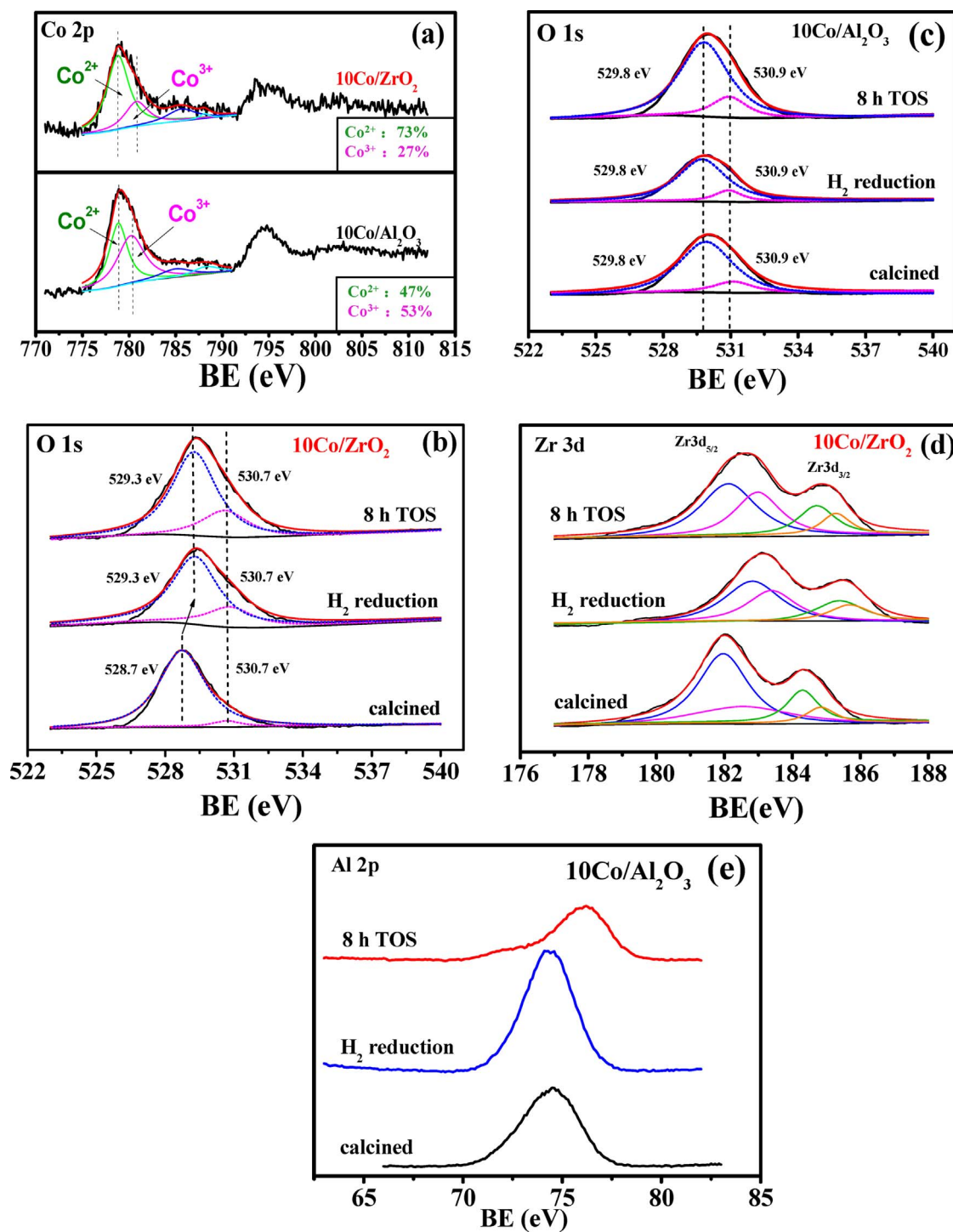
Fig. 7. (a) XPS spectra of Co 2p on the calcined catalyst precursors $10Co/ZrO_2$ (upper) and $10Co/Al_2O_3$ (down) catalysts, (b) XPS spectra of O 1 s on the $10Co/ZrO_2$, (c) XPS spectra of O 1 s on the $10Co/Al_2O_3$, (d) XPS spectra of Zr 3d on the $10Co/ZrO_2$, and (e) XPS spectra of Al 2p on the $10Co/Al_2O_3$.

product H_2O.

Fig. 7(d) depicts the XPS spectra in the Zr 3d region for Co/ZrO_2. Deconvolution was applied to the superimposed peak of Zr $3d_{5/2}$, and the results indicate the existence of two components: one due to the Zr^{4+} with lower BEs (ca. 182.0-182.8 eV) and the other to Zr^{3+} with higher BEs (ca. 182.8-183.4 eV) [89]. The ratio of $Zr^{3+}/(Zr^{3+} + Zr^{4+})$ was estimated using the integrals as well and tabulated in Table 3. Noticeably, all peaks of Zr species shift to higher BEs upon reduction, along with an increase in the ratio of $Zr^{3+}/(Zr^{3+} + Zr^{4+})$, which could be attributed to the oxygen vacancies in the zirconia lattice [90,91] and

the interaction with the Co species. The Zr 3d photoelectron spectra reveal the increase of oxygen vacancies which is consistent with the observation from the O 1 s photoelectron spectra. The oxygen vacancies on the Co/ZrO_2 catalysts detected by XPS are expected to contribute to adsorbing and activating CO_2 and H_2O.

Fig. 7(e) shows the Al 2p photoelectron spectra of samples. The Al 2p spectra of calcined catalyst precursors and reduced catalysts show a main peak at 74.2 eV. The binding energy of Al 2p in the 8 h TOS spent sample has slightly higher value relative to that of calcined catalyst precursors and reduced catalysts. This shift may be associated with the

Table 3
Summary of the XPS data for as-prepared catalyst samples.

Sample	Conditions	O_β/O_T[a]/	$Zr^{3+}/(Zr^{3+} + Zr^{4+})$/%
10Co/ZrO$_2$	Fresh calcined	4.2	28.1
	H$_2$ reduction	24.0	38.5
	8 h TOS	25.1	39.8
10Co/Al$_2$O$_3$	Fresh calcined	12.0	–
	H$_2$ reduction	12.2	–
	8 h TOS	15.8	–

[a] Ratios of O_β and O_T were calculated from area integration of O_α and O_β in O 1 s XPS spectra ($O_T = O_\alpha + O_\beta$).

formation of CoAl$_2$O$_4$.

3.6. New Co-Zr phase formation

The morphological properties of Co-based catalysts were studied by high-resolution TEM and STEM/EDS. Fig. 8(a) and (b) illustrate the EDS maps of calcined catalyst precursors and reduced Co/ZrO$_2$ catalysts, respectively. In the calcined form, the bulk Co$_3$O$_4$ particles are observed with the particle size of ca. 20 nm, which is in line with the value estimated based on XRD pattern. Upon reduction, the Co species generated the re-dispersion and the Co^0 particles become smaller and characteristically disperse on the surface of ZrO$_2$ particles. On the other hand, the Co species are widely dispersed on the Al$_2$O$_3$, which shows little variation between the calcined and reduced form, as depicted in Fig. 8(c) and (d), respectively.

In order to examine the phases of Co species and ZrO$_2$ particles, the Co/ZrO$_2$ samples in both calcined and reduced forms were examined by

TEM, and the high-resolution TEM images are presented in Figs. 9 and 10, respectively. In the calcined form, the TEM images clearly show a border between the Co$_3$O$_4$ and ZrO$_2$ particles at the interface. Interestingly, the clear border disappears upon reduction; a new phase is observed clearly at the interface. A measurement of the lattice fringe shows that the new phase has no correlation with ZrO$_2$, Co^0, or Co$_x$O$_y$. The thickness of this new phase was about 1–2 nm.

It is proposed that the oxygen vacancies exist on the partially reduced Co/ZrO$_2$. XPS results confirmed the presence of oxygen vacancies on Co/ZrO$_2$ but not on Co/Al$_2$O$_3$. From another perspective, the presence of metal nanoparticles could promote the formation of O vacancies on ZrO$_2$. Gianfranco *et al.* [92] reported that Au nanoparticles promote the formation of surface O vacancies on ZrO$_2$ by DFT. Because of this, the bonding between Co species and surface Zr atoms becomes stronger thus more stable upon reduction, which, in return, leads to the re-dispersion of Co^0 on ZrO$_2$. This may be responsible for the observed formation of the new Co-Zr phase. Moreover, such characteristic interface still exists even after 300 h TOS (see **Fig. S2**). Such a strong Co-Zr interaction also may play a crucial role in preventing the Co^0 particles from sintering. On the contrary, no any new phase of Co-Al is observed on Al$_2$O$_3$-supported catalyst in the reduced form (see **Fig. S3**). The Co sites on ZrO$_2$ are not only larger in the numbers, but also more catalytically active (higher turnover frequencies) than on Al$_2$O$_3$ (see Table 2). Therefore, the observed high activity and stability on Co/ZrO$_2$ catalysts may be associated with the newly formed Co-Zr phase during H$_2$ reduction.

3.7. Adsorption properties of catalysts

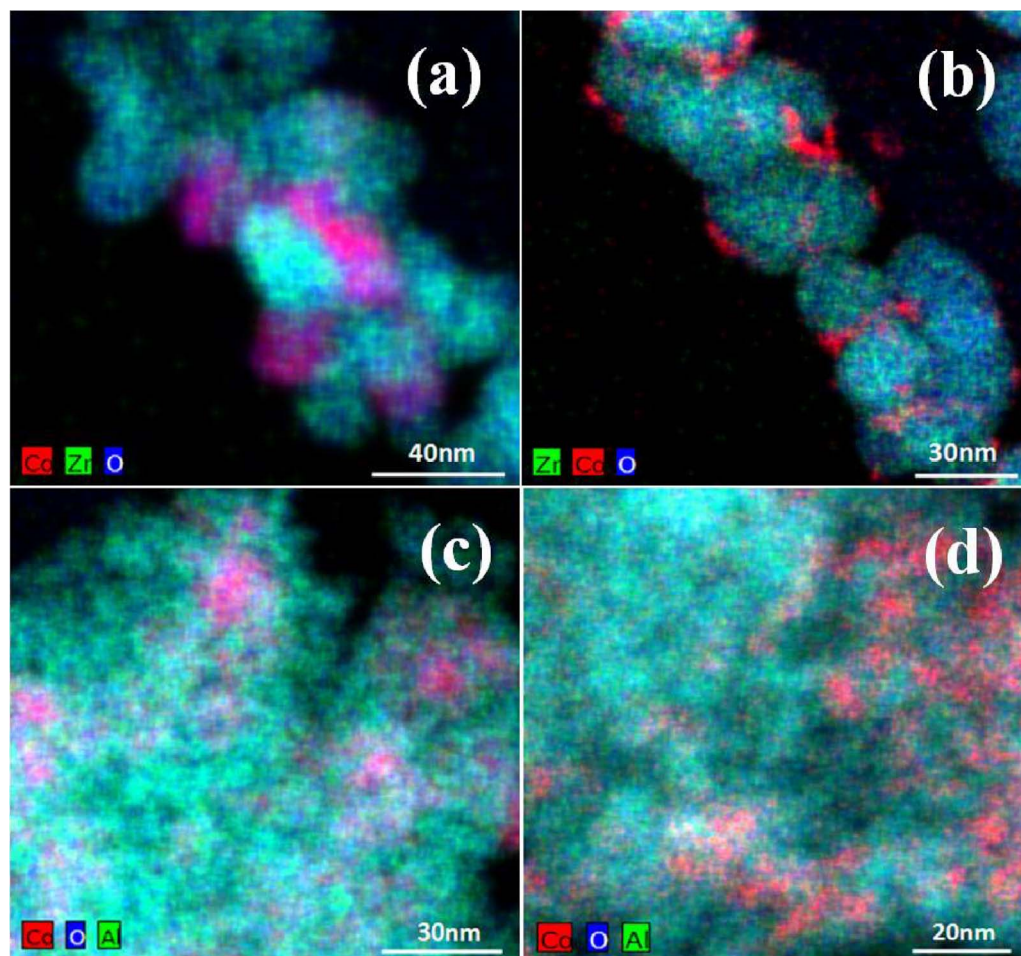The TPD profiles with CO$_2$, H$_2$, CO, NH$_3$ and CH$_4$ desorption for

Fig. 8. STEM-EDS elemental maps of (a) calcined catalyst precursors Co$_3$O$_4$/ZrO$_2$, (b) reduced catalyst Co/ZrO$_2$, (c) calcined catalyst precursors Co$_3$O$_4$/Al$_2$O$_3$, and (d) reduced catalyst Co/Al$_2$O$_3$.

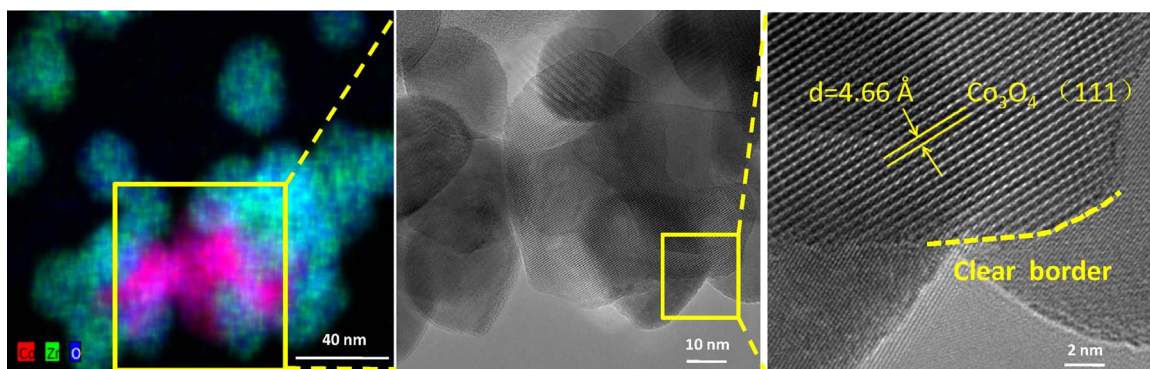**Fig. 9.** STEM-EDS maps and corresponding TEM images of calcined catalyst precursors Co_3O_4/ZrO_2.

catalysts pre-reduced at 400 °C are shown in Fig. 11, and those for catalysts pre-reduced at 550 °C are given in **Fig. S4**. The differences between TPD results of Co/ZrO_2 and Co/Al_2O_3 catalysts for both the 400 and 550 °C pre-reduced catalysts are similar. H_2-TPD profiles in both Fig. 11**(a)** and in **Fig. S4**(a) indicate that the H_2 desorption temperature over $10Co/ZrO_2$ is higher, thus the H_2 adsorption on the $10Co/ZrO_2$ is stronger than that on the $10Co/Al_2O_3$. The peak area for $10Co/ZrO_2$ is greater than that for $10Co/Al_2O_3$, which is due to the higher reducibility of $10Co/ZrO_2$.

The CO_2 adsorption properties were investigated by TPD. CO_2-TPD profiles in Fig. 11**(b)** can be divided into three regions [93,94]: 50–150 °C, 150–240 °C and > 240 °C, which correspond to weak, medium and strong adsorption, respectively [95]. CO_2 prefers to adsorb on basic sites on ZrO_2 via acid-basic interaction, and the CO_2 adsorption strength is related to the basicity of ZrO_2[94,96]. The weak basic sites are related to the surface hydroxyl group; the medium basic sites are ascribed to the metal-oxygen pairs (i.e. Zr^{4+}-O^{2-} pair); the strong basic sites are associated with the low-coordination oxygen anions. On the other hand, $10Co/Al_2O_3$ only displays a weak adsorption towards CO_2. It is likely that there exists an optimum ratio of the chemisorbed H_2 and CO_2 for CO_2 hydrogenation. The oxygen vacancies characterized by XPS can strongly absorb the oxygen atom in CO_2, which contributes to the CO_2 adsorption on ZrO_2-supported catalyst. The new phase on the Co-ZrO_2 interface possibly provides the additional adsorption sites for CO_2. This assumption is supported by the following DFT results.

The NH_3-TPD profiles are shown in Fig. 11(c). On the ZrO_2-supported catalyst, there is almost no NH_3 adsorption. On the Al_2O_3-supported catalyst, a broad desorption peak with a maximum at 150–180 °C and a shoulder at higher temperature (260–290 °C) are visible. The low temperature peak could be ascribed to weak and medium-strength acid sites, whereas the peak above 260 °C is typical of strong acid sites. Weak interactions can occur between OH groups on alumina and NH_3 through H-bond formation [97] and the strong adsorption is related to Al^{3+} cations [98,99].
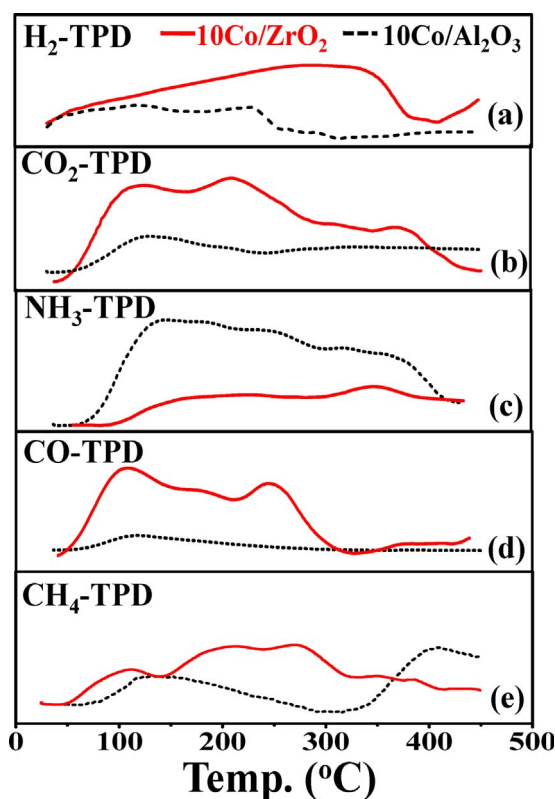

Fig. 11. The profiles of temperature programmed desorption of $10Co/ZrO_2$ and $10Co/Al_2O_3$ catalysts (a) H_2-TPD, (b) CO_2-TPD, (c) NH_3-TPD, (d) CO-TPD, (e) CH_4-TPD. The catalysts were reduced at 400 °C before TPD.
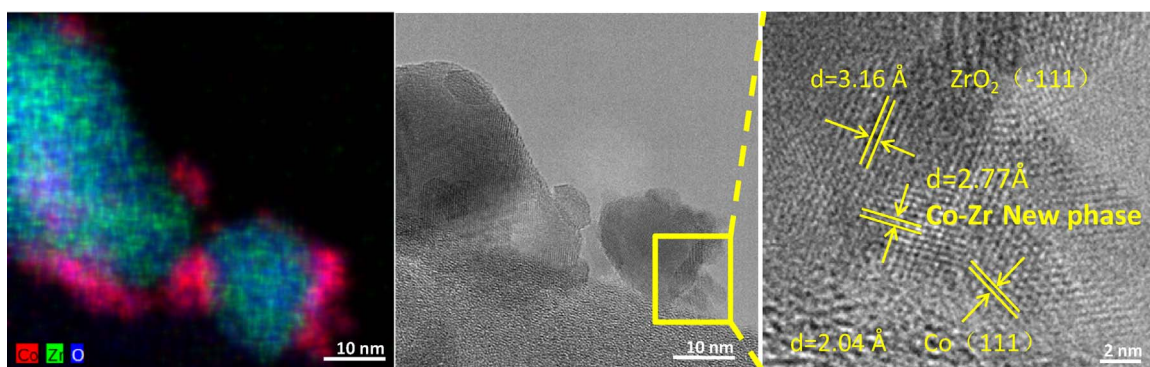

Fig. 10. STEM-EDS maps and corresponding TEM images of reduced catalyst Co/ZrO_2.

Fig. 11(d) presents the CO desorption behavior of the pre-reduced catalysts. The Al_2O_3-supported catalyst had almost no CO desorption. There are three desorption peaks on the ZrO_2-supported catalyst over the range of 50–150 °C, 150–200 °C and 200–300 °C. The higher the desorption temperature, the stronger the interaction between CO and catalyst. The oxygen vacancies characterized by XPS also contributes to the CO adsorption on ZrO_2-supported catalyst. As reported in the literature, CO is a intermediate product of CO_2 methanation [100]. The strongly adsorbed CO can undergo hydrogenation which could improve the CH_4 selectivity.

The CH_4 adsorption performance of the $10Co/ZrO_2$ and $10Co/Al_2O_3$ catalysts are shown in Fig. 11(e). The CH_4 desorption temperatures below and above 300 °C on the ZrO_2- and Al_2O_3-supported catalysts correspond to weak and strong adsorption of CH_4. More weak CH_4 adsorption on ZrO_2-supported catalyst facilitates the removal of product during CO_2 methanation.

The Co/ZrO_2 catalysts show stronger adsorption of reactants CO_2 and H_2, and of intermediate product CO compared to Co/Al_2O_3. The strong H_2 adsorption is necessary for formation of the $Co-ZrO_2$ phase and oxygen vacancies, subsequently, the oxygen vacancies can contribute to the CO_2 adsorption and activation. These characteristics should benefit the CO_2 hydrogenation.

3.8. Deactivation analysis

As discussed in Section 3.1, ZrO_2- and Al_2O_3-supported catalysts performed differently in CO_2 methanation stability. Detailed characterization suggests that the new phase formed at the interface contributes to such a significant difference. In order to clarify the reasons, the spent catalysts after 300 h TOS were analyzed by TG in the temperature range of 30–800 °C, as depicted in Fig. 12. The first peak below 200 °C for both $10Co/ZrO_2$ and $10Co/Al_2O_3$ appears at the same temperature and is due to the loss of water, except that the weight loss of the latter is more severe and rapid than the former. The spent $10Co/Al_2O_3$ shows another peak at ca. 500 °C, corresponding to the oxidation of carbon deposits. However, such oxidation is not observed on $10Co/ZrO_2$, and the weight loss is limited above 200 °C. The total weight losses of spent $10Co/ZrO_2$ and $10Co/Al_2O_3$ after 300 h TOS are 2.5 wt% and 9.3 wt%, respectively.

According to the methanation stoichiometry, converting 1 mol of CO_2 generates 2 mol of H_2O, which might lead to deactivation by water byproduct, especially at higher conversions. To evaluate the hydrothermal effect on deactivation due to byproduct water, the hydrothermal (H_2O) treatment was conducted on Co/ZrO_2 and Co/Al_2O_3 catalysts. Prior to CO_2 methanation, H_2O was pumped into the reactor (ca. 0.327 ml/min using advection pump) for 4 h after H_2 reduction at 400 °C and 3 MPa (ca. 8 h). In the subsequent step, CO_2 methanation was initiated and the resulting CO_2 conversion and CH_4 selectivity are presented in Fig. 13, along with the activity data of the catalysts
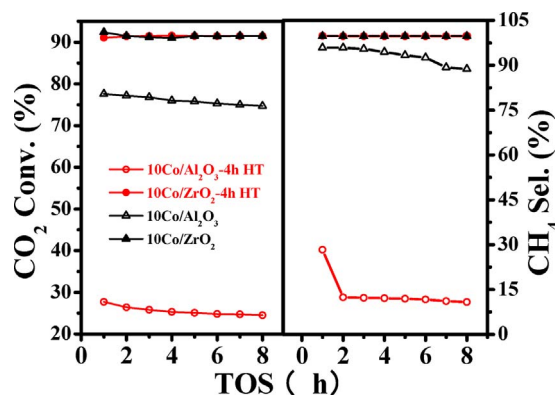

Fig. 13. CO_2 conversion (left) and CH_4 selectivity (right) over the $10Co/ZrO_2$ and $10Co/Al_2O_3$ catalysts after hydrothermal treatment.

without H_2O-hydrothermal treatment for comparison. The H_2O-treated Co/ZrO_2 exhibits similar activity and selectivity as that without H_2O treatment. In contrast, substantial losses in both conversion and selectivity can be observed clearly on the H_2O-treated Co/Al_2O_3, and the conversion is only ca. 1/3 of the catalyst without H_2O treatment. Evidently, the product H_2O can be an important cause for the observed deactivation of Al_2O_3-supported catalysts. There are also significant color change on the spent $10Co/Al_2O_3$ as depicted in **Fig. S5**. The blue color in **Figs. S5 (b)**, **(c)** and **(d)** is typical for $CoAl_2O_4$ which is consistent with the XRD results (Fig. 4). It is also noticed that the color of the spent catalyst is dependent upon the cumulated water formation, as the color grows darker from 8 h TOS **(Fig. S5 (b))** to 300 h TOS **(Fig. S5 (c))**, and the treatment with a large amount of H_2O prior to the methanation greatly accelerates the formation of $CoAl_2O_4$ **(Fig. S5 (d))**. Thus, the product H_2O promotes the formation of the inactive phase $CoAl_2O_4$, leading to the rapid deactivation of Co/Al_2O_3 catalysts.

The superior resistance to deactivation of Co/ZrO_2 catalysts can be attributed to following reason. The first reason is that the spinel structure is difficult to form on the ZrO_2 supports (Fig. 3). The other significant factor is the surface oxygen vacancies on the ZrO_2 as evidenced by Zr 3d and O 1 s photoelectron spectra. The oxygen vacancies are considered as effective for activating the product H_2O which prevents the carbon deposition from covering the active centers [101–103]. In contrast, the $CoAl_2O_4$ spinel structure is easily formed on and thus dramatically deactivates the Co/Al_2O_3 catalysts (Fig. 4). In the case of higher Co loading, the deactivation rate of Co/Al_2O_3 is slightly slower (see Fig. 2(a)), indicating that one of the deactivating ways is the decrease of active metals. Furthermore, the acid sites detected by NH_3-TPD on Al_2O_3-supported catalysts may facilitate carbon deposition, which leads to increased carbon deposits and more deactivation of the catalyst.

4. Conclusion

ZrO_2-supported Co catalyst with a proper metal loading is significantly superior over the corresponding Al_2O_3-supported Co catalyst for CO_2 methanation. The CO_2 conversion and CH_4 selectivity can be maintained at a high level even after 300 h TOS on the $10Co/ZrO_2$ catalyst which are 92.5% and 99.9%, respectively, while the corresponding values on the $10Co/Al_2O_3$ catalyst decreased sharply to 38.6% and 62.8% after 300 h, respectively. The weight loss due to carbon deposits on the spent $10Co/Al_2O_3$ catalyst is 9.3% while it is only 2.5% on the spent $10Co/ZrO_2$ catalyst. The oxygen vacancies on the Co/ZrO_2 catalysts detected by XPS, may contribute to activation of CO_2 and H_2O and resist the formation of carbon deposits.

The formation of $CoAl_2O_4$ spinel structure, which was found to be enhanced by hydrothermal effect (due to water byproduct), and the increased carbon deposition due to acid sites on Al_2O_3 contribute to
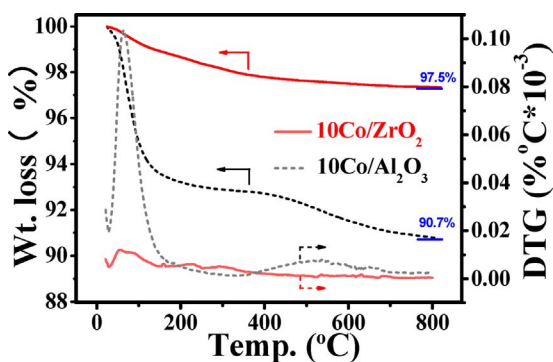

Fig. 12. The TG-DTG curves of spent $10Co/ZrO_2$ and $10Co/Al_2O_3$ catalysts after 300 h time on stream.

dramatically speeding up the deactivation of the 10Co/Al$_2$O$_3$ catalyst during CO$_2$ methanation.

Re-dispersion of Co species on the ZrO$_2$ support during the reduction by hydrogen was observed by STEM/EDS. New Co-Zr phase formed on the Co-ZrO$_2$ interface was directly observed for the first time; the Co/ZrO$_2$ catalyst exhibited high stability with high activity for CO$_2$ conversion.

The in situ XRD and H$_2$-TPR demonstrate that the reduction temperature of Co/ZrO$_2$ is much lower than that of Co/Al$_2$O$_3$, even lower than that of pure Co$_3$O$_4$. The spinel CoAl$_2$O$_4$ observed in XRD patterns is difficult to be reduced, which also leads to poor reduction of cobalt species on the 10Co/Al$_2$O$_3$. The Co^{2+} is easier conformed than the Co^{3+} in ZrO$_2$ support based on XPS.

The ZrO$_2$ support shows strong adsorption for reactant H$_2$, CO$_2$, and intermediate product CO, which benefits CO$_2$ methanation. Based on the estimated turnover frequency values, it is conjectured that the active sites on Co/ZrO$_2$ are more active than those on Co/Al$_2$O$_3$ in CO$_2$ hydrogenation.

Acknowledgement

Appendix A. Supplementary data

Supplementary data associated with this article can be found, in the online version, at http://dx.doi.org/10.1016/j.apcatb.2017.08.048.

References

[1] G.A. Meehl, W.M. Washington, W.D. Collins, J.M. Arblaster, A. Hu, L.E. Buja, W.G. Strand, H.Y. Teng, Science 307 (2005) 1769–1770.
[2] S. Saeidi, N.A.S. Amin, M.R. Rahimpour, J. CO$_2$ Util 5 (2014) 66–81.
[3] X.L. Ma, X.X. Wang, C.S. Song, J. Am. Chem. Soc. 131 (2009) 5777–5783.
[4] M.A.A. Aziz, A.A. Jalil, S. Triwahyono, A. Ahmad, Green Chem. 17 (2015) 2647–2663 (5).
[5] I. Dimitriou, P. García-Gutiérrez, R.H. Elder, R.M. Cuéllar-Franca, A. Azapagic, R.W.K. Allen, Energy Environ. Sci. 8 (2015) 1775–1789.
[6] P.G. Jessop, F. Joó, C.C. Tai, Coordin. Chem. Rev. 248 (2004) 2425–2442.
[7] S. Toshiyasu, J.C. Choi, Y. Hiroyuki, Chem.Rev 107 (2007) 2365–2387.
[8] W. Wang, S. Wang, X. Ma, J. Gong, Chem. Soc. Rev. 40 (2011) 3703–3727.
[9] C. Song, Catal. Today 115 (2006) 2–32.
[10] C. Song, Catal. Today 77 (2002) 17–49.
[11] J. Ma, N. Sun, X. Zhang, N. Zhao, F. Xiao, W. Wei, Y. Sun, Catal. Today 148 (2009) 221–231.
[12] G. Centi, S. Perathoner, Catal. Today 148 (2009) 191–205.
[13] G. Centi, S. Perathoner, Greenhouse Gases: Sci. Technol. 1 (2011) 21–35.
[14] L. Li, M. Dongsen, Y. Jun, G. Xiaoming, J. Power Sources 279 (2015) 394–404.
[15] X. Jiang, N. Koizumi, X. Guo, C. Song, Appl. Catal. B: Environ. 170–171 (2015) 173–185.
[16] W. Cai, P. Ramirez de la Piscina, J. Toyir, N. Homs, Catal. Today 242 (2015) 193–199.
[17] S. Back, H. Kim, Y. Jung, ACS Catal. 5 (2015) 965–971.
[18] J.A. Rodriguez, P. Liu, D.J. Stacchiola, S.D. Senanayake, M.G. White, J.G. Chen, ACS Catal. 5 (2015) 6696–6706.
[19] P. Gao, F. Li, H. Zhan, N. Zhao, F. Xiao, W. Wei, L. Zhong, H. Wang, Y. Sun, J. Catal. 298 (2013) 51–60.
[20] R. Satthawong, N. Koizumi, C. Song, P. Prasassarakich, Top. Catal. 57 (2014) 588–594.
[21] F. Ding, A. Zhang, M. Liu, X. Guo, C. Song, RSC Adv. 4 (2014) 8930–8938.
[22] F. Ding, A. Zhang, M. Liu, Y. Zuo, K. Li, X. Guo, C. Song, Ind. Eng. Chem. Res. 53 (2014) 17563–17569.
[23] L. Zhou, Q. Wang, L. Ma, J. Chen, J. Ma, Z. Zi, Catal. Lett. 145 (2015) 612–619.
[24] A. Westermann, B. Azambre, M.C. Bacariza, I. Graca, M.F. Ribeiro, J.M. Lopes, C. Henriques, Appl. Catal. B: Environ. 174 (2015) 120–125.
[25] D.C. Upham, A.R. Derk, S. Sharma, H. Metiu, E.W. McFarland, Catal. Sci. Technol. 5 (2015) 1783–1791.
[26] N. Shimoda, D. Shoji, K. Tani, M. Fujiwara, K. Urasaki, R. Kikuchi, S. Satokawa, Appl. Catal. B: Environ. 174 (2015) 486–495.
[27] R. Razzaq, C. Li, M. Usman, K. Suzuki, S. Zhang, Chem. Eng. J. 262 (2015) 1090–1098.
[28] S.K. Beaumont, S. Alayoglu, C. Specht, W.D. Michalak, V.V. Pushkarev, J. Guo, N. Kruse, G.A. Somorjai, J. Am. Chem. Soc. 136 (2014) 9898–9901.
[29] F. Wang, C. Li, X. Zhang, M. Wei, D.G. Evans, X. Duan, J. Catal. 329 (2015) 177–186.
[30] M.D. Porosoff, B. Yan, J.G. Chen, Energy Environ. Sci. 9 (2016) 62–73.
[31] M.S. Duyar, A. Ramachandran, C. Wang, R.J. Farrauto, J. CO$_2$ Util 12 (2015) 27–33.
[32] M.S. Duyar, M.A.A. Treviño, R.J. Farrauto, Appl. Catal. B: Environ. 168–169 (2015) 370–376.
[33] Q. Zheng, R. Farrauto, A. Chau Nguyen, Ind. Eng. Chem. Res. 55 (2016) 6768–6776.
[34] C. Janke, M.S. Duyar, M. Hoskins, R. Farrauto, Appl. Catal. B: Environ. 152–153 (2014) 184–191.
[35] K. Hashimoto, M. Yamasaki, S. Meguro, Corro. Sci. 44 (2002) 371–386.
[36] A.D. Tomsett, T. Haginwara, A. Miyamoto, T. Inui, Appl. Catal. 26 (1986) 391.
[37] K.R. Thampi, J. Kiwi, M. Gratzel, Nature 327 (1987) 506.
[38] J. Gao, Y. Wang, Y. Ping, D. Hu, G. Xu, F. Gu, F. Su, RSC Adv. 2 (2012) 2358.
[39] F. Koschany, D. Schlereth, O. Hinrichsen, Appl. Catal. B: Environ. 181 (2016) 504–516.
[40] J. Janlamool, P. Praserthdam, B. Jongsomjit, J. Nat. Gas Chem. 20 (2011) 558–564.
[41] G. Zhou, T. Wu, H. Xie, X. Zheng, Int. J. Hydrogen Energ. 38 (2013) 10012–10018.
[42] G. Zhou, T. Wu, H. Zhang, H. Xie, Y. Feng, Chem. Eng. Commun. 201 (2014) 233–240.
[43] H.H. Shin, L. Lu, Z. Yang, C.J. Kiely, S. McIntosh, ACS Catal. (2016) 2811–2818.
[44] G. Du, S. Lim, Y. Yang, C. Wang, L. Pfefferle, G. Haller, J. Catal. 249 (2007) 370–379.
[45] I. Rossetti, C. Biffi, C.L. Bianchi, V. Nichele, M. Signoretto, F. Menegazzo, E. Finocchio, G. Ramis, A. Di Michele, Appl. Catal. B: Environ. 117–118 (2012) 384–396.
[46] D. Theleritis, S. Souentie, A. Siokou, A. Katsaounis, C.G. Vayenas, ACS Catal. 2 (2012) 770–780.
[47] J.H. Kwak, L. Kovarik, J. Szanyi, ACS Catal. 3 (2013) 2449–2455.
[48] A. Karelovic, P. Ruiz, Appl. Catal. B: Environ. 113–114 (2012) 237–249.
[49] J.N. Park, E.W. McFarland, J. Catal. 266 (2009) 92.
[50] J.H. Kwak, L. Kovarik, J. Szanyi, ACS Catal. 3 (2013) 2094–2100.
[51] D.W. Gordon, H.B. Calvin, J. Catal. 87 (1984) 352–362.
[52] J. Liu, D. Cui, J. Yu, F. Su, G. Xu, Chinese J. Chem. Eng. 23 (2015) 86–92.
[53] M.A.A. Aziz, A.A. Jalil, S. Triwahyono, R.R. Mukti, Y.H. Taufiq-Yap, M.R. Sazegar, Appl. Catal. B: Environ. 147 (2014) 359–368.
[54] Z.Q. Wang, Z.N. Xu, S.Y. Peng, M.J. Zhang, G. Lu, Q.S. Chen, Y. Chen, G.C. Guo, ACS Catal. 5 (2015) 4255–4259.
[55] G.R. Johnson, A.T. Bell, ACS Catal. (2015) 100–114.
[56] J. Zeng, J. Qiu, Z. Li, P. Pavaskar, S.B. Cronin, ACS Catal. 4 (2014) 3512–3516.
[57] C.G. Visconti, L. Lietti, E. Tronconi, P. Forzatti, R. Zennaro, E. Finocchio, Appl. Catal. A: Gen. 355 (2009) 61–68.
[58] S. Kattel, W. Yu, X. Yang, B. Yan, Y. Huang, W. Wan, P. Liu, J.G. Chen, Angew. Chem. Int. Ed 55 (2016) 1–7.
[59] Y. Liu, K. Fang, J. Chen, Y. Sun, Green Chem. 9 (2007) 611.
[60] S. Sokolov, E.V. Kondratenko, M.M. Pohl, A. Barkschat, U. Rodemerck, Appl. Catal. B: Environ. 113–114 (2012) 19–30.
[61] V. Nichele, M. Signoretto, F. Menegazzo, A. Gallo, V. Dal Santo, G. Cruciani, G. Cerrato, Appl. Catal. B: Environ. 111–112 (2012) 225–232.
[62] A.M. Abdel-Mageed, D. Widmann, S.E. Olesen, I. Chorkendorff, J. Biskupek, R.J. Behm, ACS Catal. 5 (2015) 6753–6763.
[63] P. Kangvansura, H. Schulz, A. Suramitr, Y. Poo-arporn, P. Viravathana, A. Worayingyong, A. Mat, Sci. Eng. B 190 (2014) 82–89.
[64] R. Oukaci, A.H. Singleton, J.G. Goodwin Jr., Appl. Catal. A: Gen. 186 (1999) 129–144.
[65] K. Tanabe, T. Yamaguchi, Catal. Today 20 (1994) 185–197.
[66] S. Foraita, J.L. Fulton, Z.A. Chase, A. Vjunov, P. Xu, E. Barath, D.M. Camaioni, C. Zhao, J.A. Lercher, Chem. Eur. J. 21 (2015) 2423–2434.
[67] J. Ye, C. Liu, D. Mei, Q. Ge, ACS Catal. 3 (2013) 1296–1306.
[68] T. Yamaguchi, Catal. Today 20 (1994) 199–218.
[69] X. Yang, S. Kattel, S.D. Senanayake, J.A. Boscoboinik, X. Nie, J. Graciani, J.A. Rodriguez, P. Liu, D.J. Stacchiola, J.G. Chen, J. Am. Chem. Soc. 137 (2015) 10104–10107.
[70] Y. Pan, C. Liu, T.S. Wiltowski, Q. Ge, Catal. Today 147 (2009) 68–76.
[71] S. Yin, Q. Ge, Catal. Today 194 (2012) 30–37.
[72] Y. Wang, Y. Su, M. Zhu, L. Kang, Int. J. Hydrogen Energ. 40 (2015) 8864–8876.
[73] T. Kropp, J. Paier, J. Sauer, J. Am. Chem. Soc. 136 (2014) 14616–14625.
[74] S. Akamaru, T. Shimazaki, M. Kubo, T. Abe, Appl. Catal. A: Gen. 470 (2014) 405–411.
[75] A.L. Kustov, A.M. Frey, K.E. Larsen, T. Johannessen, J.K. Nørskov, C.H. Christensen, Appl. Catal. A: Gen. 320 (2007) 98–104.
[76] M.P. Andersson, T. Bligaard, A. Kustov, K.E. Larsen, J. Greeley, T. Johannessen, C.H. Christensen, J.K. Nørskov, J. Catal. 239 (2006) 501–506.
[77] A.T. Bell, Science 299 (2003) 1688–1691.
[78] W.Z. Li, H. Huang, H.J. Li, W. Zhang, H. Liu, langmuir 24 (2008) 8358–8366.
[79] G. Jacobs, J.A. Chaney, P.M. Patterson, T.K. Das, B.H. Davis, Appl. Catal. A: Gen. 264 (2004) 203–212.

[80] S. Vada, A. Hoff, E. Adnanes, D. Schanke, A. Holme, Top. Catal. 2 (1995) 155–162.
[81] B. Jongsomjit, J. Panpranot, J.G. Goodwin, J. Catal. 204 (2001) 98–109.
[82] Y. Zhang, M. Shinoda, N. Tsubaki, Catal. Today 93–95 (2004) 55–63.
[83] J. Zhang, J. Chen, J. Ren, Y. Sun, Appl. Catal. A: Gen. 243 (2003) 121–133.
[84] J. Zhang, J. Chen, J. Ren, Y. Li, Y. Sun, Fuel 82 (2003) 581–586.
[85] X. Wang, H. Shi, J.H. Kwak, J. Szanyi, ACS Catal. 5 (2015) 6337–6349.
[86] Y. Yao, Y. Cai, G. Wu, F. Wei, X. Li, H. Chen, S. Wang, J. Hazard. Mater. 296 (2015) 128–137.
[87] J. Zhu, J. Yang, Z.F. Bian, J. Ren, Y.M. Liu, Y. Cao, H.X. Li, H.Y. He, K.N. Fan, Appl. Catal. B: Environ. 76 (2007) 82–91.
[88] Z. He, W. Que, J. Chen, Y. He, G. Wang, J. Phys. Chem. Solids 74 (2013) 924–928.
[89] H. Li, J. Ren, X. Qin, Z. Qin, J. Lin, Z. Li, RSC Adv. 5 (2015) 96504–96517.
[90] G.S. Wu, L.C. Wang, Y.M. Liu, Y. Cao, W.L. Dai, H.Y. He, K.N. Fan, Appl. Surf. Sci. 253 (2006) 974–982.
[91] A.G. Sato, D.P. Volanti, D.M. Meira, S. Damyanova, E. Longo, J.M.C. Bueno, J. Catal. 307 (2013) 1–17.
[92] A.R. Puigdollers, G. Pacchioni, ChemCatChem 9 (2017) 1119–1127.
[93] H. Wang, M. Wang, W. Zhang, N. Zhao, W. Wei, Y. Sun, Catal. Today 115 (2006) 107–110.
[94] V.K. Díez, C.R. Apesteguía, J.I. Di Cosimo, Catal. Today 63 (2000) 53–62.
[95] C. Zhong, X. Guo, D. Mao, S. Wang, G. Wu, G. Lu, RSC Adv. 5 (2015) 52958–52965.
[96] Z. Liu, J.A. Cortés-Concepción, M. Mustian, M.D. Amiridis, Appl. Catal. A: Gen. 302 (2006) 232–236.
[97] M. Turco, G. Bagnasco, C. Cammarano, P. Senese, U. Costantino, M. Sisani, Appl. Catal. B: Environ. 77 (2007) 46–57.
[98] P.J. Chupas, C.P. Grey, J. Catal. 224 (2004) 69–79.
[99] C. Morterra, G. Magnacca, Catal. Today 27 (1996) 497–532.
[100] J. Ren, H. Guo, J. Yang, Z. Qin, J. Lin, Z. Li, Appl. Surf. Sci. 351 (2015) 504–516.
[101] H. Wang, J. Ye, Y. Liu, Y. Li, Y. Qin, Catal. Today 129 (2007) 305–312.
[102] S.Q. Chen, H. Wang, Y. Liu, . Int. J. Hydrogen Energy 34 (2009) 7995–8005.
[103] X. Wang, Q. Liu, J. Jiang, G. Jin, H. Li, F. Gu, G. Xu, Z. Zhong, F. Su, Catal. Sci. Technol. 6 (2016) 3529–3543.